

# Compressed Sensing Based Synthetic Transmit Aperture Imaging: Validation in a Convex Array Configuration

Jing Liu, Qiong He, and Jianwen Luo, *Senior Member, IEEE*

**Abstract**—According to the linear acoustic theory, the channel data of a plane wave emitted by a linear array is a linear combination of the full data set of synthetic transmit aperture (STA). Combining this relationship with compressed sensing (CS), a novel CS based ultrasound beamforming strategy, named compressed sensing based synthetic transmit aperture (CS-STA), was previously proposed to increase the frame rate of ultrasound imaging without sacrificing the image quality for a linear array. In this paper, assuming linear transfer function of a pulse-echo ultrasound system, we derived and applied the theory of CS-STA for a slightly curved array and validated CS-STA in a convex array configuration. Computer simulations demonstrated that, in the convex array configuration, the normalized root-mean-square error between the beamformed radio-frequency data of CS-STA and STA was smaller than 1% while CS-STA achieved four-fold higher frame rate than STA. In addition, CS-STA was capable of achieving good image quality at depths over 100 mm. It was validated in phantom experiments by comparing CS-STA with STA, multielement synthetic transmit aperture (ME-STA), and the conventional focused method (focal depth = 110 mm). The experimental results showed that STA and CS-STA performed better than ME-STA and the focused method at small depths. At the depth of 110 mm, CS-STA, ME-STA, and the focused methods improved the contrast and contrast-to-noise ratio of STA. The improvements in CS-STA are higher than those in ME-STA but lower than those in the focused mode. These results can also be observed qualitatively in the *in vivo* experiments on the liver of a healthy male volunteer. The CS-STA method is thus proved to increase the frame rate and achieve high image quality at full depth in the convex array configuration.

**Index Terms**—Compressed sensing, convex array, ultrasound.

## I. INTRODUCTION

FOR practical use, the classical Nyquist sampling frequency usually results in a big size of the sampled signal, which restricts the data storage and transportation. Although some postprocessing method such as data compression is helpful to relieve this problem, it cannot decrease the data size of the original sampled signal. To solve this problem more fundamentally, compressed sensing (CS) was

proposed [1]. CS states that if a signal  $\mathbf{x} \in \mathbf{R}^n$  is sparse or has a sparse representation in a basis  $\Psi \in \mathbf{R}^{n \times n}$ , it can be recovered from its linear combinations  $\mathbf{y} \in \mathbf{R}^m$  ( $m < n$ ) with fewer samples [1], [2]. With this advantage, CS has been applied to several fields. The applications include but are not limited to magnetic resonance imaging [3], radar imaging [4], computed tomography [5], photoacoustic tomography [6], [7], and single pixel camera [8]. The keys to these applications are the design of the compressive sampling strategy in specific applications and the recovery of the original signal afterward.

Recently, CS has also been adopted in ultrasound imaging [9]–[21]. The challenge of applying CS to ultrasound imaging lies in the design of the sampling strategy that is suitable for ultrasound data acquisition. Once the CS sampling strategy is determined, the recovering stage afterward can be accomplished by applying the CS reconstruction algorithms. The sampling strategy of CS applications in ultrasound imaging can be roughly grouped into three categories: compressive sampling in the fast time direction, compressive sampling in the slow time direction, and inverse scattering problem (ISP) solving. The first strategy is useful for reduction of the data size and the latter two are capable of achieving high-frame-rate or ultrafast imaging, which is beneficial for transient elastography [22], blood flow imaging [23], [24], cardiac imaging [25], [26], and so on.

In ultrasound imaging, the sampling frequency is about four to ten times of the central frequency of the ultrasound transducer [27]. As the central frequency is typically several megahertz, the sampling frequency is usually tens of megahertz, which results in a big size of the ultrasound radio-frequency (RF) signal. To lower down the data size, the RF signal can be sampled in a CS way by multiplying the measurement matrix  $\Phi \in \mathbf{R}^{m \times n}$  with the original RF signal  $\mathbf{x} \in \mathbf{R}^n$ . Different measurement matrixes produce different sampling strategies. In these cases, compressive sampling is applied in the depth direction (i.e., fast time direction). Achim *et al.* [28] chose a random Gaussian measurement matrix to subsample the postbeamformed RF signal. To subsample the prebeamformed RF signal, and Liebgott *et al.* [16] and Friboulet *et al.* [29] constructed a measurement matrix with columns having an entry one at random positions and zero elsewhere. A similar matrix was used as one of the sampling strategies in [13] and [30] to subsample the postbeamformed RF signal. Tur *et al.* [12] applied the finite rate of innovation model to ultrasound imaging and developed a sampling

Manuscript received January 16, 2017; accepted March 9, 2017. Date of publication March 14, 2017; date of current version March 1, 2018. This work was supported in part by the National Natural Science Foundation of China under Grant 81471665, Grant 81561168023, Grant 61271131, and Grant 61322101, and in part by the National Key Research and Development Program of China under Grant 2016YFC0102201 and Grant 2016YFC0104705. (Corresponding author: Jianwen Luo).

The authors are with the Department of Biomedical Engineering, School of Medicine, Tsinghua University, Beijing 100084, China (e-mail: luo\_jianwen@tsinghua.edu.cn).

Digital Object Identifier 10.1109/TUFFC.2017.2682180

strategy to sample the partial Fourier coefficients of the analog prebeamformed demodulated baseband signal directly. In their method, the measurement matrix was a partial Fourier matrix. Wagner *et al.* [14] and Chernyakova and Eldar [17] extended this paper and sampled the partial Fourier coefficients of beamformed RF signal directly.

Since a typical ultrasound sequence transmits ultrasound waves sequentially, one way to improve the frame rate of ultrasound imaging is to apply compressive sampling in the direction in which the transmit event repeats (i.e., slow time direction). As each ultrasound image is composed of a number of image lines, Quinsac *et al.* [13], [30] designed a sampling strategy in the slow time direction by selecting the image lines randomly. It can be also extended to 3-D ultrasound imaging to increase the frame rate [20]. In their methods, each row of the measurement matrix had an entry one at random positions and zero elsewhere. According to the linear acoustic theory, the channel data of a plane wave firing with a linear array transducer is a linear combination of the full channel data set of synthetic transmit aperture (STA) [31]. The linear coefficients are equal to the transmit apodization of the plane wave firing. According to this relationship, we proposed a novel beamforming strategy, named CS based STA (CS-STA), to sample the full STA channel data set in the slow time direction by transmitting randomly apodized plane waves [21]. Each transmit apodization composed the corresponding row of the measurement matrix. Simulations, phantom experiments and *in vivo* experiments proved that this method was capable of improving the frame rate and image quality at the same time with the linear array configuration.

Another CS way to improve the frame rate is ISP solving. Different from sampling the received RF signal in the fast time or slow time direction, the CS based ISP solving method samples the parameter to be imaged with a set of sampling kernel functions, which form the measurement matrix. The sampled signal is exactly the RF signal received by the array elements. As the sampled signal can be acquired from a single plane wave transmit, this method is capable of achieving ultrafast imaging. Different kernel functions produce different imaging frameworks. Assuming that the imaging parameter related compressibility was sparse, Schiffner and Schmitz [11] reconstructed it by choosing the Green's functions as the kernel functions. The image quality of this method was further improved by compensating the effects of absorption and dispersion [32]. In this approach, the Green's functions were derived based on the ultrasound wave equation in the frequency domain. On the contrary, the Green's functions can also be calculated in the time domain. Based on the spatial point spread function, David *et al.* [18] modeled this process and reconstructed the reflectivity coefficients in the time domain. They also revealed the equivalent relationship between this process and delay-and-sum (DAS) beamforming operation. From the DAS point of view, Shen *et al.* [15] and Wang *et al.* [19] derived the measurement matrix and reconstructed the intensities of the backscatter targets in the frequency and time domains, respectively.

In this paper, we applied CS-STA to a convex array, which is widely used in abdominal imaging and obstetrics, and usually

has a large imaging depth over 100 mm. Different from the linear array, the convex array has a curved surface. As a result, the linear relationship between the channel data set of STA and that of plane wave firings in the linear array [21] needs to be extended for the convex array with more assumptions. In this paper, assuming that the convex array is slightly curved, the linear relationship between the channel data set of STA and that of diverging wave firings is derived in theory. Simulations demonstrated that CS-STA is capable of recovering the channel data set of STA in the convex array configuration with a smaller number of firings. To investigate if the assumption of the slightly curved convex array is applicable for a real convex array, CS-STA was compared with several methods in phantom and *in vivo* experiments with a real convex array in an ultrasound system. The results demonstrated that CS-STA is capable of achieving good image quality at full depth in the convex array configuration.

This paper is organized as follows. Section II briefly describes the CS theory and the CS-STA method. Sections III and IV present the simulations and phantom experiments of CS-STA with a convex array, respectively. Section V presents the *in vivo* experiments on the liver of a healthy male volunteer. At last, Sections VI and VII discuss and conclude this paper, respectively.

## II. THEORY STUDY

### A. Compressed Sensing

Assuming a signal  $\mathbf{x} \in \mathbf{R}^n$  or its projection in some basis is sparse (i.e., most entries of the signal are zero), the CS theory states that it can be recovered from its linear measurements  $\mathbf{y} \in \mathbf{R}^m$  ( $m < n$ ) with high probability [1]. It should be noted that the length ( $m$ ) of the measurements is typically smaller than that ( $n$ ) of the original signal in CS applications. In mathematical language

$$\mathbf{x} = \Psi \mathbf{v} \quad (1)$$

$$\mathbf{y} = \Phi \mathbf{x}. \quad (2)$$

Equation (1) means that the signal  $\mathbf{x}$  can be represented sparsely in the basis  $\Psi \in \mathbf{R}^{n \times n}$ , and  $\mathbf{v} \in \mathbf{R}^n$  is its sparse representation.  $\Psi$  is also called the sparse basis. Equation (2) shows the sampling process in CS, and  $\Phi \in \mathbf{R}^{m \times n}$  is called the measurement matrix. Substituting (1) into (2), we can obtain

$$\mathbf{y} = \Theta \mathbf{v} \quad (3)$$

where  $\Theta = \Phi \Psi$ .

With the prior knowledge that  $\mathbf{v}$  is sparse, it can be reconstructed by solving the following  $l_0$  minimization problem [33]:

$$\hat{\mathbf{v}} = \arg \min_{\mathbf{v} \in \mathbf{R}^n} \|\mathbf{v}\|_0 \quad \text{s.t. } \mathbf{y} = \Theta \mathbf{v} \quad (4)$$

where  $\|\mathbf{v}\|_0$  is the  $l_0$  pseudonorm of  $\mathbf{v}$  and denotes the number of nonzero entries of  $\mathbf{v}$ . Minimizing  $\|\mathbf{v}\|_0$  keeps the sparsity of  $\mathbf{v}$ . To obtain the sparse solution of  $\mathbf{v}$ ,  $\Theta$  must satisfy the property named uniform uncertainty principle [34] or restricted isometry property (RIP) [2], [35]. RIP indicates that all subsets of  $s$  (i.e., the number of nonzero entries) columns taken

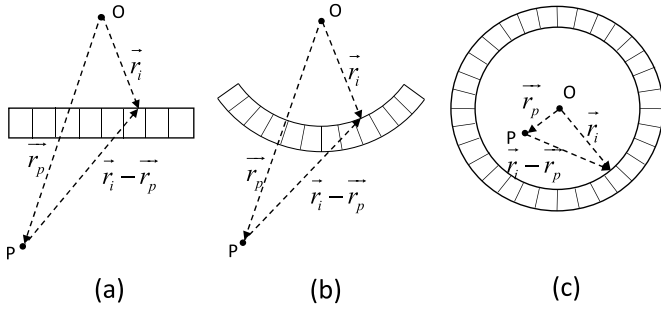


Fig. 1. Spatial coordinates for different arrays. (a)–(c) Linear, convex, and ring arrays, respectively. Point  $O$  is the origin of the coordinate system, which can be arbitrarily selected.

from  $\Theta$  are nearly orthogonal. This property is satisfied with overwhelming probability when  $\Psi$  is an orthogonal basis and  $\Phi$  obeys a random distribution, such as Gaussian or Bernoulli distribution. Please refer to [2] for more applicable  $\Phi$ .

The  $l_0$  minimization problem is usually NP-hard (nondeterministic polynomial hard), but it can be solved suboptimally with greedy algorithms, such as orthogonal matching pursuit [36]. When more restrictive bounds are imposed on the isometry constant of RIP, the  $l_1$  minimization is capable of approaching the solution of the  $l_0$  minimization and therefore the sparse solution of  $\mathbf{v}$  can be approximated well by solving the following problem [1]:

$$\hat{\mathbf{v}} = \arg \min_{\mathbf{v} \in \mathbb{R}^n} \|\mathbf{v}\|_1 \quad \text{s.t. } \mathbf{y} = \Theta \mathbf{v} \quad (5)$$

where  $\|\mathbf{v}\|_1$  is the  $l_1$  norm of  $\mathbf{v}$ . This problem can be solved with some convex optimization algorithms, such as basis pursuit [37].

In actual world, the sampled signal is usually polluted by noise, and then the problem is recast to

$$\hat{\mathbf{v}} = \arg \min_{\mathbf{v} \in \mathbb{R}^n} \|\mathbf{v}\|_1 \quad \text{s.t. } \|\mathbf{y} - \Theta \mathbf{v}\|_2 \leq \varepsilon \quad (6)$$

which can be solved with basis pursuit denoising algorithms [37]. In (6), the constraint condition renders that the  $l_2$  norm of the error between  $\mathbf{y}$  and  $\Theta \mathbf{v}$  is smaller than a tolerated error  $\varepsilon$ . Moreover,  $\mathbf{v}$  in the actual world is not exactly sparse but compressible (i.e., most entries of  $\mathbf{v}$  are very small and the sorted coefficients of  $\mathbf{v}$  decay very fast). For this case, (6) only gives the approximate solution of  $\mathbf{v}$  by keeping its  $s$  largest entries. Once  $\mathbf{v}$  is achieved,  $\mathbf{x}$  can be easily obtained from (1).

### B. Compressed Sensing Based Synthetic Transmit Aperture

Consider that a point  $P$  with reflectivity coefficient  $f(\vec{r}_p)$  is placed in front of an arbitrarily shaped array with  $n$  elements. Fig. 1 shows this situation with linear, convex, and ring arrays, respectively.  $\vec{r}_i$  and  $\vec{r}_p$  are the positions of the  $i^{\text{th}}$  element of the array and point  $P$ , respectively. Assuming a linear ultrasound system, it is well known that the pulse-echo signal received by the  $j^{\text{th}}$  element can be expressed as [38]

$$s(\vec{r}_j, t) = \frac{1}{c_0^2} \frac{\partial^2 v_{\text{pe}}(t)}{\partial t^2} \underset{t}{*} h_{\text{tx}}(\vec{r}_p, t) \underset{t}{*} h_{\text{rx}}(\vec{r}_j, \vec{r}_p, t) \underset{r}{*} f(\vec{r}_p) \quad (7)$$

where  $v_{\text{pe}}(t)$  is the pulse-echo electromechanical impulse response including the excitation function,  $h_{\text{tx}}(\vec{r}_p, t)$  and  $h_{\text{rx}}(\vec{r}_j, \vec{r}_p, t)$  are the transmit and receive spatial impulse responses for point  $P$ , respectively,  $c_0$  is the speed of sound and  $*$  and  $*$  denote the temporal and spatial convolution operations, respectively.

For simplicity, the transducer elements are considered as point sources, and therefore, the spatial impulse response of a planar transducer with  $n$  elements for point  $P$  can be calculated as [39]

$$h(\vec{r}_p, t) = \sum_{i=1}^n a_i \frac{\delta\left(t - \frac{|\vec{r}_i - \vec{r}_p|}{c_0}\right)}{|\vec{r}_i - \vec{r}_p|} \quad (8)$$

where  $i$  is the element index,  $a_i$  is the apodization amplitude applied to the  $i^{\text{th}}$  element,  $\delta(t)$  is the Dirac function and  $|\vec{r}_i - \vec{r}_p|$  is the distance from point  $P$  to the  $i^{\text{th}}$  element. However, if a curved transducer is used, which is the case of convex and ring arrays as Fig. 1(b) and (c) shows, a second order diffraction term will be introduced into (8) [40]. In this paper, we assume that the transducer is slightly curved and large compared with the ultrasound wavelength and then (8) will be a good approximation for the curved transducer [40]. If only the  $i^{\text{th}}$  element is active and the corresponding apodization amplitude is 1, the spatial impulse response of this element for point  $P$  is given by

$$h(\vec{r}_i, \vec{r}_p, t) = \frac{\delta\left(t - \frac{|\vec{r}_i - \vec{r}_p|}{c_0}\right)}{|\vec{r}_i - \vec{r}_p|}. \quad (9)$$

Now, consider the pulse-echo signal received by the  $j^{\text{th}}$  element for STA, in which only the  $i^{\text{th}}$  element is active in the  $i^{\text{th}}$  firing (i.e., transmit event) and the corresponding apodization amplitude is 1.  $h_{\text{tx}}(\vec{r}_p, t)$  and  $h_{\text{rx}}(\vec{r}_j, \vec{r}_p, t)$  can be calculated from (9). By substituting these two terms into (7), the pulse-echo signal  $s_{\text{STA}}(\vec{r}_i, \vec{r}_j, t)$  received by the  $j^{\text{th}}$  element for the  $i^{\text{th}}$  firing can be obtained as

$$s_{\text{STA}}(\vec{r}_i, \vec{r}_j, t) = \frac{1}{c_0^2} \frac{\partial^2 v_{\text{pe}}(t)}{\partial t^2} \underset{t}{*} \frac{\delta\left(t - \frac{|\vec{r}_i - \vec{r}_p|}{c_0}\right)}{|\vec{r}_i - \vec{r}_p|} \underset{t}{*} \frac{\delta\left(t - \frac{|\vec{r}_j - \vec{r}_p|}{c_0}\right)}{|\vec{r}_j - \vec{r}_p|} \underset{r}{*} f(\vec{r}_p). \quad (10)$$

Similar to the plane wave firing for a linear array, other shaped arrays (such as a convex array or ring array) can be implemented to transmit ultrasound wave by firing all elements simultaneously. Considering that the wavefront varies with the shape of the array, it is called as diverging wave (DW) for a convex array in this paper. If the apodization amplitude applied to the  $i^{\text{th}}$  element for the  $k^{\text{th}}$  DW firing is  $a_{k,i}$ ,  $h_{\text{tx}}(\vec{r}_p, t)$  and  $h_{\text{rx}}(\vec{r}_j, \vec{r}_p, t)$  can be calculated from (8) and (9), respectively. By substituting these two terms into (7), the pulse-echo signal  $s_{\text{DW}}(k, \vec{r}_j, t)$  received by the  $j^{\text{th}}$  element for the  $k^{\text{th}}$  DW firing

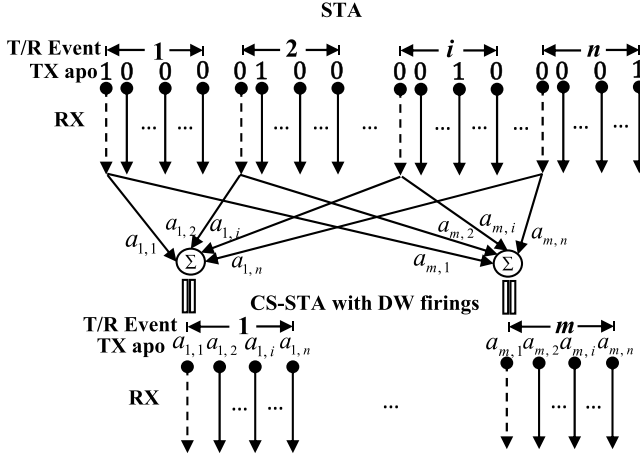


Fig. 2. Illustration of the relationship between STA and DW firings. For an  $n$ -element array, STA and CS-STA consist of  $n$  and  $m$  ( $m < n$ ) transmit/receive events, respectively. For STA, a single element is active in each transmit. For CS-STA, DW firing (with all element active) is used in the transmit. The transmit apodizations (0 or 1 for STA firing,  $a$  for DW firing) are denoted by TX apo. The receive event is denoted by RX (with all elements receiving for both STA and CS-STA) and the received channel data are presented as the upright arrows. The dashed arrows are used to describe that the channel data received by the first channel of a DW firing is the weighted summation of those received by the same channel of all STA firings. The weights are the corresponding transmit apodization in the DW firing.

can be obtained as

$$s_{PW}(k, \vec{r}_j, t) = \frac{1}{c_0^2} \frac{\partial^2 v_{pe}(t)}{\partial t^2} * \sum_{i=1}^n a_{k,i} \frac{\delta\left(t - \frac{|\vec{r}_i - \vec{r}_p|}{c_0}\right)}{|\vec{r}_i - \vec{r}_p|} * \frac{\delta\left(t - \frac{|\vec{r}_j - \vec{r}_p|}{c_0}\right)}{|\vec{r}_j - \vec{r}_p|} * f(\vec{r}_p). \quad (11)$$

By comparing (10) and (11), it can be found that

$$s_{PW}(k, \vec{r}_j, t) = \sum_{i=1}^n a_{k,i} s_{STA}(\vec{r}_i, \vec{r}_j, t). \quad (12)$$

That is to say, the channel data received by the  $j^{\text{th}}$  element in the  $k^{\text{th}}$  DW firing is a linear combination of those in STA firings and the linear coefficients are exactly the transmit apodization applied to the DW firing. This linear relationship is derived based on the assumption that each element is a point source. Actually, the element is not a point source but has a spatial extent (typically rectangular shape). It can be considered as a collection of point sources. In this condition, the spatial impulse responses of each element for point  $P$  is not expressed as (9) or the second term on the right side of (8) but its integral over the surface of this element. Nevertheless, the spatial extents of the elements do not change the linear relationship established by (12), because the same integral operations are applied on its both sides.

A more explicit illustration is shown in Fig. 2. Assuming that the transducer transmits  $m$  ( $m < n$ ) DWs and samples the pulse-echo signals  $s_{PW}(k, \vec{r}_j, t)$  and  $s_{STA}(\vec{r}_i, \vec{r}_j, t)$  at frequency  $f_s$ , (12) can be rewritten in the form of

matrix-vector multiplication as

$$\begin{bmatrix} s_{PW}\left(1, \vec{r}_j, \frac{q}{f_s}\right) \\ \vdots \\ s_{PW}\left(k, \vec{r}_j, \frac{q}{f_s}\right) \\ \vdots \\ s_{PW}\left(m, \vec{r}_j, \frac{q}{f_s}\right) \end{bmatrix} = \begin{bmatrix} a_{1,1} & a_{1,2} & \cdots & a_{1,i} & \cdots & a_{1,n} \\ \vdots & \vdots & & \ddots & & \vdots \\ a_{k,1} & a_{k,2} & \cdots & a_{k,i} & \cdots & a_{k,n} \\ \vdots & \vdots & & \ddots & & \vdots \\ a_{m,1} & a_{m,2} & \cdots & a_{m,i} & \cdots & a_{m,n} \end{bmatrix} \times \begin{bmatrix} s_{STA}\left(\vec{r}_1, \vec{r}_j, \frac{q}{f_s}\right) \\ s_{STA}\left(\vec{r}_2, \vec{r}_j, \frac{q}{f_s}\right) \\ \vdots \\ s_{STA}\left(\vec{r}_i, \vec{r}_j, \frac{q}{f_s}\right) \\ \vdots \\ s_{STA}\left(\vec{r}_n, \vec{r}_j, \frac{q}{f_s}\right) \end{bmatrix}. \quad (13)$$

Equation (13) has the same form as (2) but with the specific meaning of  $\mathbf{x}$ ,  $\mathbf{y}$  and  $\Phi$ . The  $q^{\text{th}}$  sample of the channel data received by the  $j^{\text{th}}$  element for each DW firing is an entry of the linear measurements  $\mathbf{y}$ . A total of  $m$  DW firings are used to form  $\mathbf{y}$  in CS-STA. The  $q^{\text{th}}$  sample of the channel data received by the  $j^{\text{th}}$  element of each STA firing is an entry of the original signal  $\mathbf{x}$ . A total of  $n$  STA firings are used. As defined in (11),  $a_{k,i}$  is the apodization amplitude applied to the  $i^{\text{th}}$  element for the  $k^{\text{th}}$  DW firing. Comparing (13) with (2), it can be found that  $a_{k,i}$  forms the entries of the measurement matrix  $\Phi$ . Therefore, (13) can be considered as a CS problem. Since  $\Phi$  in (2) usually obeys a random distribution, to adapt the data acquisition in ultrasound imaging,  $\Phi$  in (13) can be designed to obey a continuous uniform random distribution whose entries range between 0 and 1, i.e.,  $\Phi \sim U(0, 1)$ .

Assuming  $\mathbf{x}$  in this instance can be represented sparsely, CS-STA is capable of recovering the full STA channel data set with a smaller number of DW firings. That is how CS-STA works. First, the channel data set of  $m$  DW firings with the transmit apodizations specified by  $\Phi$  are acquired. Second, the linear measurements  $\mathbf{y}$  are formed by extracting the samples of  $m$  firings at the same receive element and sample index; and the corresponding original signal  $\mathbf{x}$ , which is the component of full STA channel data set, is recovered by solving the optimization problem as (6) describes using CS reconstruction algorithms. This process is repeated for all the receive elements and samples to recover the full STA channel data set. Finally, an STA beamforming method is used to obtain the beamformed data and the ultrasound image. In practice,  $\Phi$  can be designed in advance and then written to the hardware. The workflow and MATLAB pseudocode for the recovery of the full STA data set from the measurement signals obtained with CS-STA is provided in the Appendix.

As the shape of the array does not change the linear combination relationship between the channel data set of



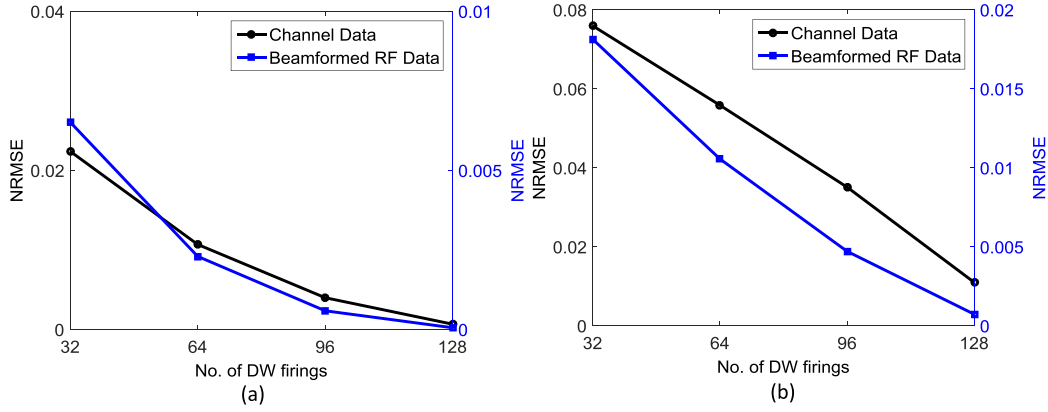


Fig. 3. NRMSE with different numbers of DW firings for the simulated (a) point and (b) cyst phantoms. The black and blue lines denote the NRMSE of the channel and beamformed RF data, respectively.

STA firing and that of DW firing with the above-mentioned assumptions, CS-STA can be applicable for any shaped array, such as linear array, convex array, and ring array.

### III. SIMULATIONS

#### A. Simulation Setup

To investigate if the full STA channel data set of a convex array transducer can be recovered from a smaller number of DW firings, a 128-element convex array transducer with a pitch of 0.47 mm was simulated in the Field II environment [41]. The radius and open angle were 61 mm and  $56^\circ$ , respectively. The transducer was excited by a 3.125 MHz Hanning window weighted sinusoidal wave with two cycles to image the point and cyst phantom with no acoustic attenuation. In the simulated point phantom, three columns of point targets were placed along different angular directions. The distance between consecutive points in each column was 15 mm. In the simulated cyst phantom, three hyperechoic regions and three anechoic cyst regions were placed in an  $80 \times 100 \text{ mm}^2$  (lateral  $\times$  axial) space, in which  $1 \times 10^5$  scatterers distributed uniformly. The received channel data were sampled at 100 MHz in Field II simulations and then were decimated to 12.5 MHz (i.e., four times of the central frequency).

For CS-STA, the channel data sets of different numbers of randomly apodized DW firings were simulated to recover the full STA channel data set. The recovery procedure was carried out by solving (6) with the SPGL1 solver [42]–[44]. The transmit apodization or measurement matrix  $\Phi$  was implemented as Section II-B described. To guarantee the sparsity, the *sym8* wavelet was chosen to construct the sparse basis  $\Psi$ . After recovering the STA channel data set, an STA beamforming technique was applied to obtain the beamformed RF data. Considering the element directivity, a modified STA beamforming [45] was used in this paper. The recovery performance of CS-STA with  $m$  DW firings (referred to as CS $m$ -STA) would be compared with the true STA data.

To study the recovery performance of CS-STA in a noisy environment, Gaussian noise at different signal-to-noise

ratio (SNR) levels (i.e., 10, 20, 30, 40, and 50 dB) was added to the backscatter echoes of CS32-STA, CS64-STA, and CS96-STA for the simulated cyst phantom. The reconstruction parameters and beamforming parameters were the same as in the noise-free conditions.

#### B. Simulation Results

To quantify the recovery error, the normalized root-mean-square error of channel (NRMSE<sub>ch</sub>) and beamformed RF data (NRMSE<sub>bf</sub>) between CS $m$ -STA and STA were calculated, respectively, as in (14), shown at the bottom of the next page, and

$$\text{NRMSE}_{\text{bf}} = \frac{\sqrt{\frac{1}{N_l N_s} \sum_{i=1}^{N_l} \sum_{q=1}^{N_s} (r f'_{\text{bf}}(l_i, s_q) - r f_{\text{bf}}(l_i, s_q))^2}}{\max_{i,q} |r f_{\text{bf}}(l_i, s_q)|}. \quad (15)$$

In (14),  $\text{rf}_{\text{ch}}(e_i, r_j, p_q)$  and  $\text{rf}'_{\text{ch}}(e_i, r_j, p_q)$  denoted the STA channel data (i.e., prebeamformed RF data) and its recovered version, respectively,  $e_i, r_j$  and  $p_q$  were the indexes of the active transmit element, receive element and RF sample, respectively, and  $N_e, N_r$ , and  $N_p$  were the number of transmit elements, number of receive elements and number of pre-beamformed RF samples for each image line, respectively. The symbols in (15) had similar meanings.  $\text{rf}_{\text{bf}}(l_i, s_q)$  and  $\text{rf}'_{\text{bf}}(l_i, s_q)$  were the beamformed RF data of STA and CS-STA, respectively,  $l_i$  and  $s_q$  were the image line and beamformed RF sample indexes, and  $N_l$  and  $N_s$  were the number of image lines and number of beamformed RF samples for each line, respectively.

Fig. 3 shows the NRMSE<sub>ch</sub> and NRMSE<sub>bf</sub> with different numbers of DW firings for the point and cyst phantoms. As shown, for both phantoms the NRMSEs decrease as the number of DW firings increases. This can be explained by that the CS reconstruction algorithm performs better when the length of measurements (i.e., the number of DW firings in CS-STA) is larger. Fig. 3 also shows that the NRMSEs for the point phantom are smaller than those for the cyst phantom. As will be discussed later, this is because the signal from the point phantom can be represented more sparsely,

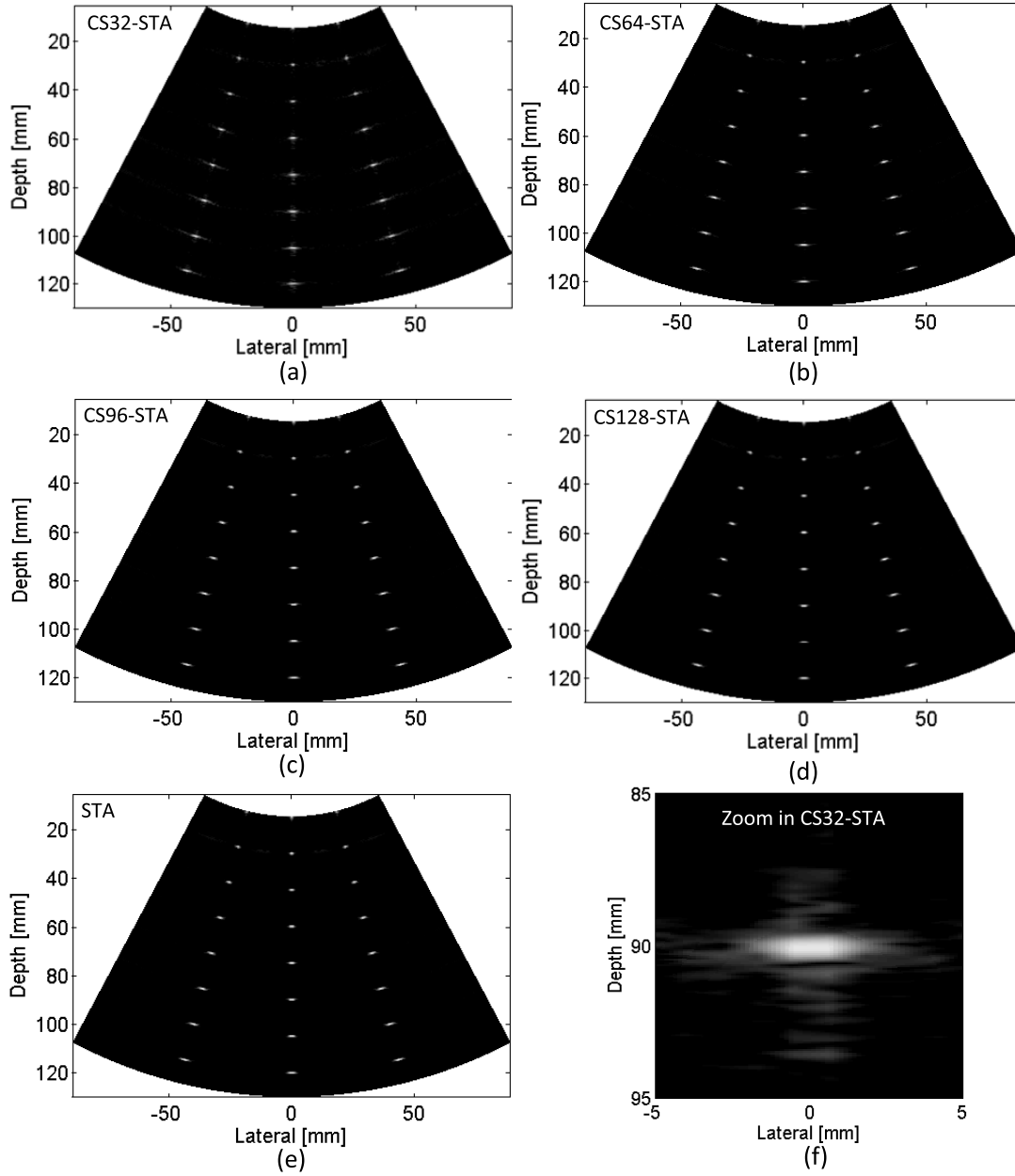


Fig. 4. B-mode images of CS-STA and STA for the simulated point phantom with a 50-dB dynamic range. (f) Zoomed-in view of (a) CS32-STA image.

which improves the performance of CS reconstruction. As can also be observed in Fig. 3, the  $\text{NRMSE}_{\text{bf}}$  is smaller than the  $\text{NRMSE}_{\text{ch}}$ . This is probably the consequence of the average effect of the beamforming operation.

The effect of the number of DW firings on the performance of CS-STA can be seen more clearly from the B-mode images in Figs. 4 and 5. When 32 firings are applied, the CS32-STA images are polluted with artifacts, which are visible along the axial direction of the

point phantom [i.e., above or below the point targets in Fig. 4(f)] and in the anechoic region of the cyst phantom as Fig. 5(f) shows. However, when the number of firings increases, these artifacts are nearly invisible in the CS64-STA, CS96-STA, and CS128-STA images. Fig. 6 shows the axial and lateral profiles of the point spread functions (PSFs) for the point at (0, 90 mm). As shown, the side lobes of CS $m$ -STA are closer to those of STA when  $m$  increases while the main lobes of CS $m$ -STA are nearly the same as those of STA.

$$\text{NRMSE}_{\text{ch}} = \frac{\sqrt{\frac{1}{N_e N_r N_p} \sum_{i=1}^{N_e} \sum_{j=1}^{N_r} \sum_{q=1}^{N_p} (r f'_{\text{ch}}(e_i, r_j, p_q) - r f_{\text{ch}}(e_i, r_j, p_q))^2}}{\max_{i,j,q} |r f_{\text{ch}}(e_i, r_j, p_q)|} \quad (14)$$

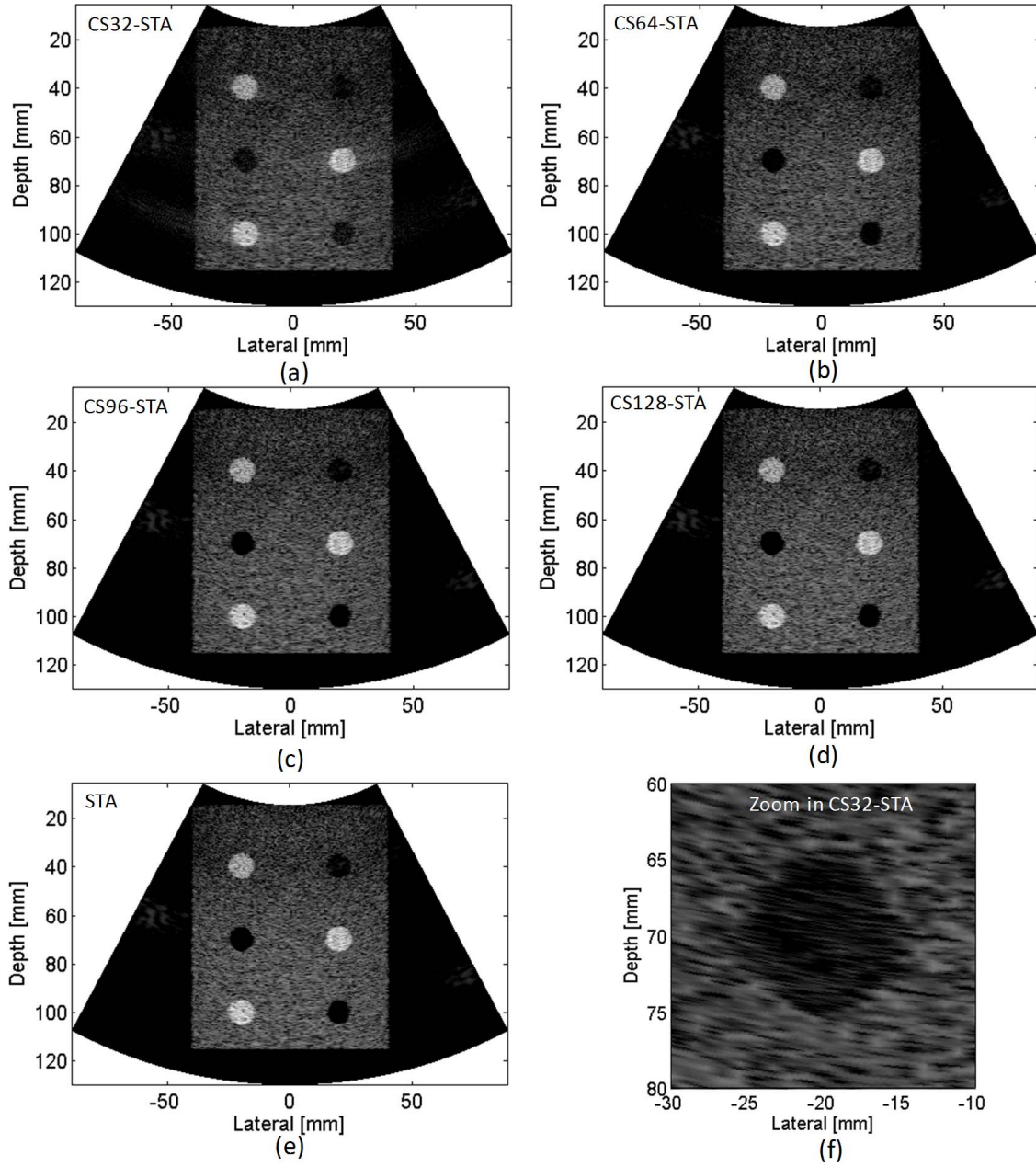


Fig. 5. B-mode images of CS-STA and STA for the simulated cyst phantom with a 50-dB dynamic range. (f) Zoomed-in view of (a) CS32-STA image.

The axial and lateral resolutions at this point are calculated by measuring the  $-6$  dB width of the corresponding PSF profiles. The axial resolutions of STA and  $CSm$ -STA are all equal to 0.43 mm. The lateral resolution of CS32-STA is 1.79 mm, which is slightly worse than those of CS64-STA (1.68 mm), CS96-STA (1.62 mm), CS128-STA (1.58 mm), and STA (1.58 mm). In addition, when  $m$  is 32, most of the side-lobe amplitudes in the axial profile are above  $-40$  dB and higher than those in the lateral profile. That is why the artifacts are more visible in the axial direction for CS32-STA in Fig. 4(a) and (f).

Fig. 7 shows the  $NRMSE_{bf}$  between CS-STA and STA at different SNR levels. As shown, the  $NRMSE_{bf}$  decreases with

the increase of SNR. When the SNR increases to 20 dB, the NRMSEs of CS-STA with different numbers of firings are very close to those in the noise-free conditions. When the SNR is higher than 30 dB, the NRMSEs are nearly the same as in the noise-free conditions. It demonstrates that CS-STA achieves similar reconstruction performance in the Gaussian noise and noise-free environments. This is reasonable, because the  $l_2$  norm constraint in (6) restrains the Gaussian noise to some extent.

#### IV. PHANTOM EXPERIMENTS

The simulations have proved that CS-STA is capable of recovering the full STA channel data set of a convex array

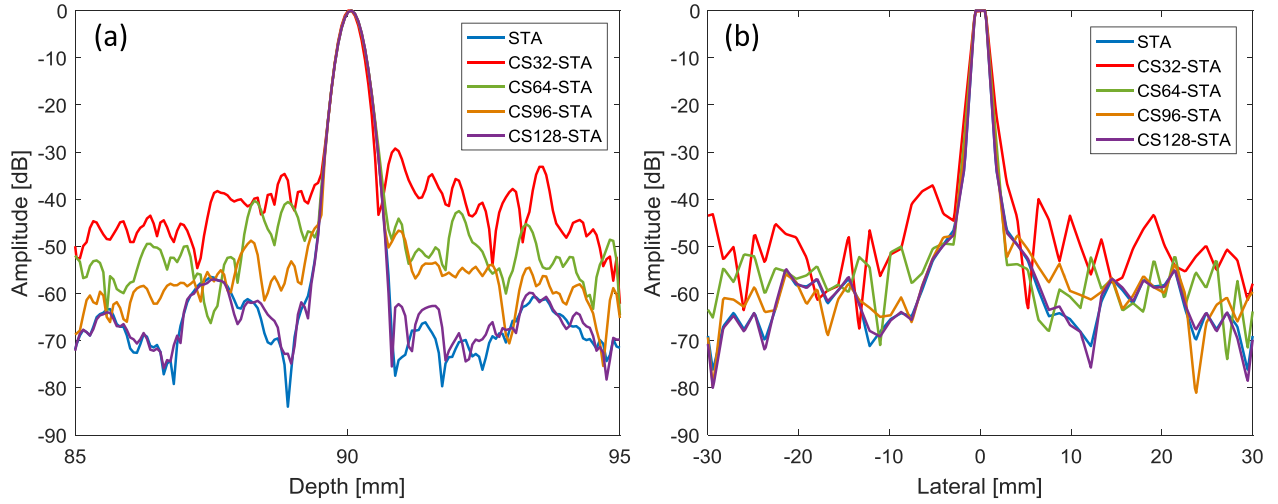


Fig. 6. Point spread function profiles for the simulated point phantom. (a) Axial and (b) lateral profile at the depth of 90 mm.

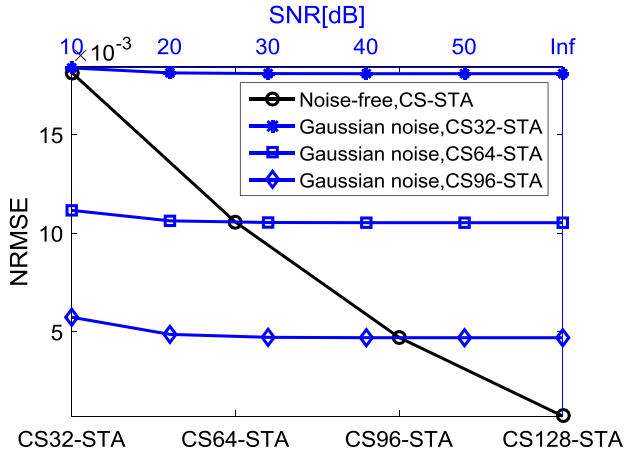


Fig. 7. Normalized NRMSE between the beamformed RF data of STA and CS-STA for the simulated cyst phantom with different SNR levels, respectively. The black curve denotes the NRMSEs of the beamformed RF data of STA and CS-STA with different firings without noise. Blue curves denoted the NRMSEs of the beamformed RF data between STA and CS-STA with different SNR levels. Inf indicates an infinite SNR (i.e., noise-free conditions).

with a smaller number of firings. However, it needs to be noted that the simulations are implemented with Field II simulator based on the same assumptions as Section II describes on the derivation of the spatial impulse response of a curved transducer. The assumption may not hold in the real acquisition system. In this section, we conducted phantom experiments to validate the performance of CS-STA with a research system.

#### A. Experimental Setup

A C5-2 convex array transducer (Shenzhen JiaRui Co., Shenzhen, China) with the same parameters as the simulated convex array was connected to a Vantage 256 system (Verasonics Inc., Redmond, WA, USA) to scan a CIRS 040GSE model tissue mimicking phantom (CIRS, Norfolk, VA, USA). The image quality of CS-STA was compared with STA, the conventional focused mode, and multielement-STA (ME-STA) [31].

STA and the focused mode were implemented with 128 firings and the other three modes were implemented with

a smaller number of firings to increase the frame rate. All these modes were applied with 12 V voltage and used the same time gain compensation (TGC) setup. The focal depth and transmit  $f$ -number for the focused mode were 110 mm and 2, respectively. For CS-STA, the transducer transmits 32 and 64 DWs with random apodizations as Section II-B described. For ME-STA, 11 elements were activated at the same time and then shifted to the next 11 elements with a nine-element or seven-element overlap for 60 or 30 firings, respectively. These implementations would produce nearly two-fold or four-fold increase in the frame rate compared with STA or the focused mode. Similar to  $CS_m$ -STA,  $ME_m$ -STA denotes ME-STA with  $m$  firings.

The same STA beamforming method [45] as used in the simulations was performed. For ME-STA, a similar beamforming method was applied [46] by approximating the 11-element subaperture of the convex array as a small linear array. For the focused mode, the receive  $f$ -number was 1.5 and a rectangular window was used as the receive apodization.

#### B. Experimental Results

Fig. 8 shows the B-mode images of different methods. There are some strip artifacts in the shallow regions of the ME-STA images [Fig. 8(c) and (d)]. This is the consequence of “transmit beam separation” of subaperture in ME-STA [46]. At small depth, the hyperechoic and hypoechoic regions are all clear. However, the wires in the focused mode are visually wider than those in STA, ME-STA, and CS-STA. In convex array applications, the image quality at the large depth is relatively more important. In the bottom left region which is outside the phantom and thus is expected to be dark, there is visible noise in the STA and ME30-STA images (marked as yellow rectangular boxes). Fig. 9 shows the zoomed-in view images around the depth of 110 mm. As shown, the boundaries of the hyperechoic (e.g., the region marked with yellow arrows) and hypoechoic regions at the depth of 110 mm are much clearer in STA, the focused mode, and CS-STA than in ME-STA. Still from Fig. 9, as the red arrows mark, the STA image is polluted



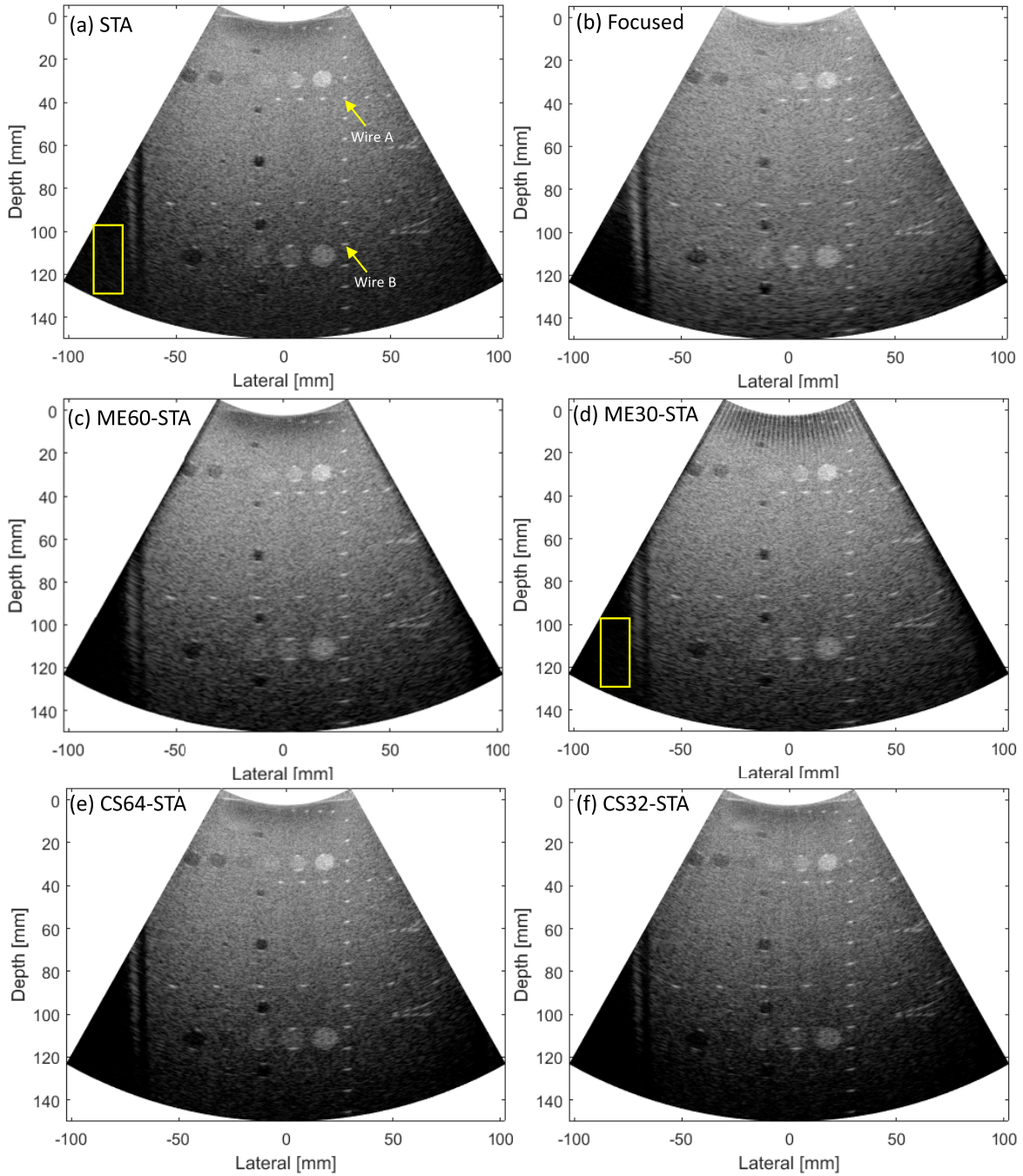


Fig. 8. B-mode images of different methods for the CIRS phantom with a 70-dB dynamic range.

with visible noise, which disappears to some extent in the focused mode, ME-STA, and CS-STA. From the qualitative B-mode results, it appears that CS-STA achieves good resolution at full depth and good detection capability at the large depth as well.

The axial and lateral PSF profiles for two wires [marked as wires A and B in Fig. 8(a)] at different depths are shown in Fig. 10. As shown, for wires A and B, the main lobe widths of the axial PSF profiles are nearly the same for different modes. However, the main lobe widths of the lateral PSF profiles are different for different modes. For wire A which is out of the focal zone of the focused mode, CS-STA

and STA achieve the smallest main lobe width. For wire B which is in the focal zone of the focused mode, CS-STA, STA, and the focused mode achieve the smallest main lobe width. The corresponding axial and lateral resolutions for wires A and B are also calculated. As shown in Table I, the axial resolutions for wires A and B are around 0.4 mm for different modes. For wire A, the lateral resolutions of CS-STA and STA are about 1.1 mm, which is about 0.5 mm smaller than those of ME-STA and the focused mode. For wire B, the lateral resolutions of CS-STA, STA, and the focused mode are about 2 mm, which is about 0.8 mm smaller than that of ME-STA. From these

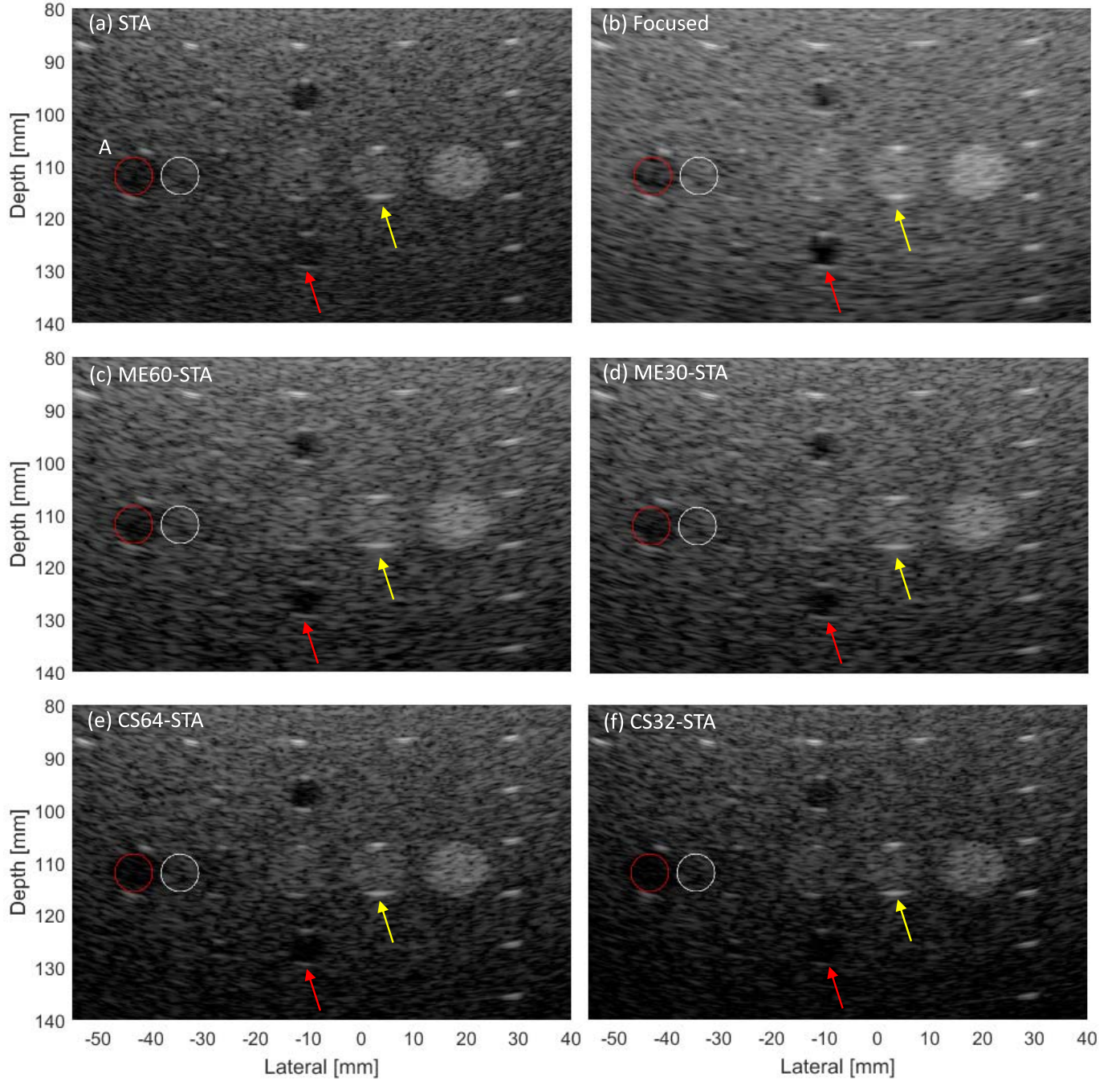


Fig. 9. Zoomed-in view of Fig. 8 at large depth.

resolution results, it can be concluded that with a smaller number of firings, CS-STA is capable of achieving good resolution at full depth.

To quantify the image quality at the large depth, the contrast-to-noise ratio (CNR) and contrast of a hypoechoic region were calculated as

$$\text{CNR} = 20 * \log 10 \left( \frac{|\mu_c - \mu_b|}{\sqrt{\sigma_c^2 + \sigma_b^2}} \right) \quad (16)$$

$$\text{contrast} = |\mu_c - \mu_b| \quad (17)$$

where  $\mu_c$  and  $\sigma_c$  were the mean and standard deviation (SD) of the B-mode image in the region of interest (ROI),  $\mu_b$ ,

and  $\sigma_b$  were the mean and SD of the B-mode image in their background region.

ROI A and its corresponding background region are marked as red and white circles, respectively, in Fig. 9(a). The CNR and contrast results are shown in Table I and they are in accordance with the qualitative observations. First, STA (0.66 dB) and the focused mode (2.88 dB) achieve the lowest and highest CNR with 128 firings, respectively. With about two-fold higher frame rate, ME60-STA and CS64-STA achieve about 0.6- and 1.6-dB higher CNR than STA, respectively. Moreover, with about four-fold higher frame rate, ME30-STA, and CS32-STA achieve about 0.07- and 0.5-dB higher CNR than STA, respectively. The contrast results have

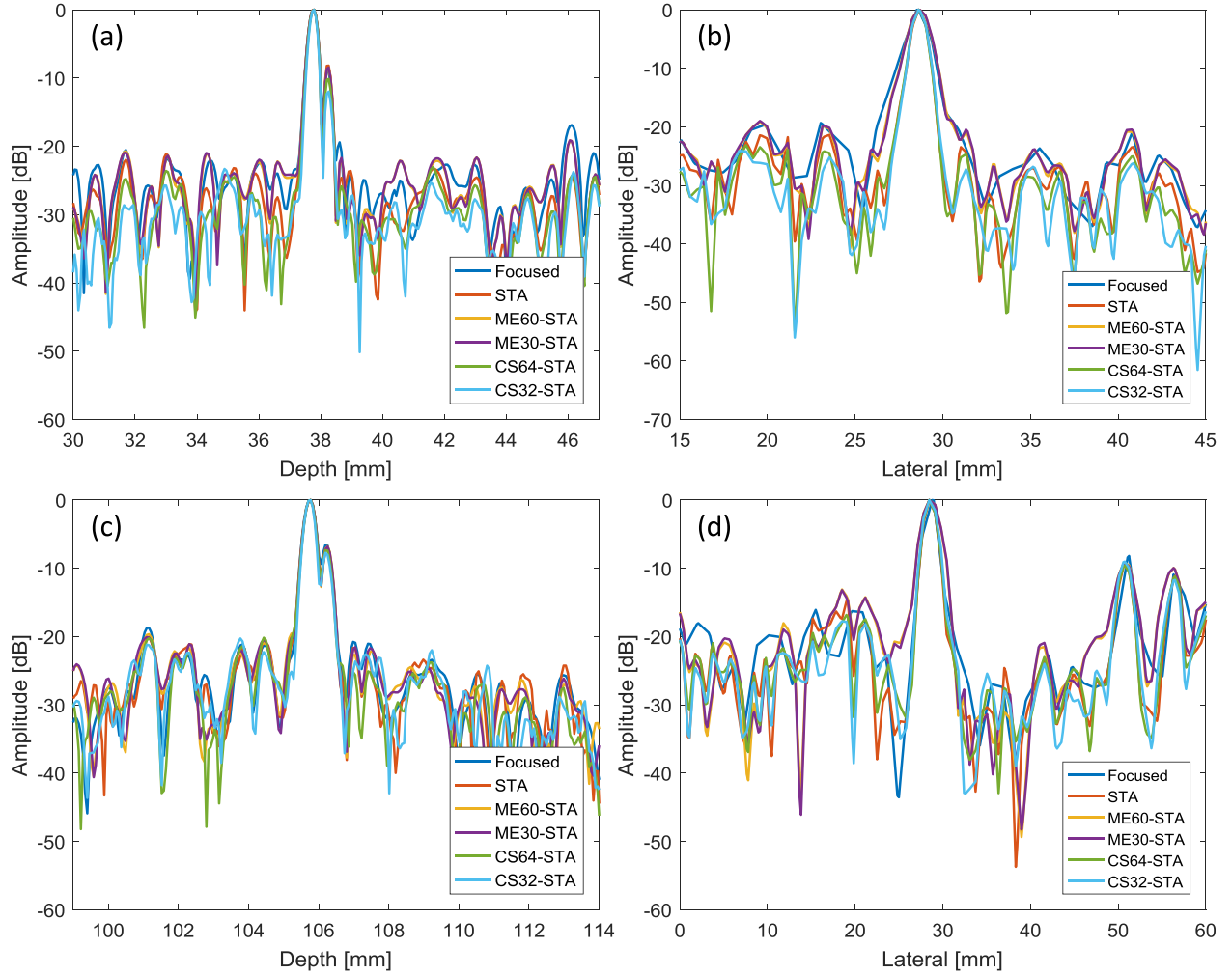


Fig. 10. (a) Axial and (b) lateral PSF profiles for wire A, and (c) axial and (d) lateral PSF profiles for wire B.

TABLE I  
AXIAL AND LATERAL RESOLUTIONS (mm) FOR WIRES A AND B, AND CNR (dB) AND CONTRAST FOR ROI A WITH DIFFERENT METHODS

Method	Axial resolution [mm]		Lateral resolution [mm]		CNR [dB]	Contrast [dB]
	Wire A	Wire B	Wire A	Wire B		
STA	0.40	0.44	<b>1.09</b>	<b>1.95</b>	0.66	7.71
Focused	0.41	0.45	1.64	<b>1.93</b>	<b>2.88</b>	<b>10.39</b>
CS32-STA	0.36	0.40	<b>1.10</b>	<b>2.14</b>	1.18	8.19
CS64-STA	0.38	0.42	<b>1.09</b>	<b>2.00</b>	<b>2.27</b>	<b>9.23</b>
ME30-STA	0.41	0.43	1.63	2.84	0.73	8.12
ME60-STA	0.41	0.43	1.63	2.81	1.29	9.78

the same trend as the CNR results for these imaging modes. From these quantitative results at the large depth, it can be found that with higher frame rate, both ME-STA and CS-STA are capable of improving the CNR and contrast of STA. Moreover, the improvements are higher in CS-STA than in ME-STA. However, the improvements of both ME-STA and CS-STA are not as significant as the focused mode

because the focal depth of the focused mode is set at 110 mm.

## V. *IN VIVO* EXPERIMENTS

As described in Section II-B, the full STA channel data set is recovered by solving (6) using CS reconstruction algorithms. As shown in Section III-B, the  $l_2$  norm constraint in this model



is capable of suppressing Gaussian noise. However, Gaussian noise only imperfectly reflects the effective noise affecting in practice the real ultrasound data. This effect has been studied in the phantom experiments in Section IV. As shown, with more realistic noise from the acquisition system and CIRS phantom, CS-STA achieves good image quality and performs well. However, the *in vivo* condition is much more complicated. For example, the object is usually nonstationary, which is very different from the phantom. For the CS-STA case, we reconstruct the STA image by transmitting dozens of DWs. If there is motion during these DW transmissions, the reconstruction may fail.

In this section, we conducted the *in vivo* experiments on the liver of a healthy male volunteer. The experimental setup was the same as the phantom experiments. To ensure that different methods can acquire images at the same location, these methods were programmed sequentially in the same sequence and the volunteer was asked to hold the breath during the data acquisition to minimize the motion caused by respiration. Nevertheless, there may still be motion of liver vessels produced by heart beats.

The results are shown in Fig. 11. By comparing the images of STA, the focused mode, ME-STA, and CS-STA, it is found that all of them show the boundary of liver and vessels clearly. However, these images are a little different. First, there are some strip artifacts in the near field of the ME-STA images, especially for ME30-STA [Fig. 11(d)]. These strip artifacts even affect the visualization of the muscle fibers [marked as yellow arrows in Fig. 11] close to the skin in the ME30-STA image. As explained in Section IV-B, they are the consequence of the “transmit beam separation” of ME-STA. These muscle fibers in the focused mode are not as clear as those in the STA, ME60-STA, and CS-STA images. That is because they are far away from the focal region (110 mm) of the focused mode. Second, there is visible noise in the CS32-STA image [marked with red arrow in Fig. 11(f)], which is in accordance with the simulation results shown in Fig. 5(a). At last, as the yellow circles mark, there is some visible noise in the STA image at large depths and the mean noise power (MNP) of the image data in this region is about 580. In addition, this region is brighter in ME-STA than in the focused mode and CS-STA. It may be noise as the bottom-left region in Fig. 11 shows, and the MNPs for ME30-STA, ME60-STA, CS32-STA, CS64-STA, and the focused mode are about 534, 400, 306, 136, and 135, respectively. These qualitative visualizations and MNPs are in agreement with the quantitative results of phantom experiments in Section IV. From the above-mentioned results, it can be concluded that the CS-STA method is still feasible even with the motion of liver vessels caused by heart beats. Besides, CS64-STA is capable of achieving good image quality with a smaller number of firings in this condition.

## VI. DISCUSSION

### A. Discussion About the Results

The simulation results show that, up to a tolerable error, CS-STA is capable of reconstructing the full STA channel

data set with a smaller number of firings in the noise-free or Gaussian noise conditions. Moreover, the phantom and *in vivo* experiments demonstrate that CS-STA outperforms STA at the large depth in the real noisy environment. It is considered as the consequence of higher transmit energy of DW firings in CS-STA. With higher energy of DW firings, CS-STA is capable of reconstructing the full STA channel data set at higher SNR, especially at large depths. Since the beamforming procedure is the same for STA and CS-STA, the SNR of the beamformed RF data is quantified to evaluate the signal quality.

To calculate the SNR, 20 postbeamformed images of the CIRS phantom were obtained. The ultrasound signal and noise for each pixel were the mean and the SD of these 20 images, respectively [22]. The SNR for each pixel was calculated as

$$\text{SNR} = 10 * \log_{10} \left( \frac{\text{signal}^2}{\text{noise}^2} \right). \quad (18)$$

The mean SNR of the hyperechoic region around the 110-mm depth was calculated. To guarantee the reliability of the SNR results, the same phantom was scanned in three positions by moving the probe moderately. The mean SNRs are shown in Fig. 12. As shown, STA and CS32-STA achieve almost the same SNR, and CS64-STA achieves the highest SNR. The SNR of CS64-STA is about 3-dB higher than that of STA.

The similar SNR of STA and CS32-STA is slightly inconsistent with the CNR and contrast results (i.e., the CNR and contrast of CS32-STA are higher than those of STA). This is related to the way of calculating the SNR and the noise type in the real conditions. The simulation results demonstrate that the CS reconstruction algorithm introduces recovery error. This error is low even in the Gaussian noise environment because of the  $l_2$  constraint. However, the noise is non-Gaussian in the real conditions. As a result, the noise will not be perfectly restrained through the  $l_2$  constraint and therefore the recovery error will be larger. Moreover, since the noise is time dependent, the introduced recovery error varies with time. For the successive 20 images used in the SNR calculation, the recovery error of each image is different. When the recovery error is large enough, the SD of the 20 images (i.e., noise) will increase thus yielding a lower the SNR. However, only one image is used in the calculation of the CNR and contrast. Therefore, there is no issue about the raised SD introduced by the recovery error.

### B. CS-STA Performance

Although CS-STA is demonstrated to be capable of recovering the full STA channel data set with a smaller number of DW firings in the simulations and achieve good image quality in the phantom and *in vivo* experiments, this method may produce some artifacts. As the CS32-STA images in Fig. 4(a) and (f) show, there are visible artifacts along the axial and lateral directions. In the phantom experiments, these kinds of artifacts may not affect the detection of targets, but they make the uniform background a little nonuniform on the CS32-STA B-mode image [see the region around (−25, 40 mm) of the



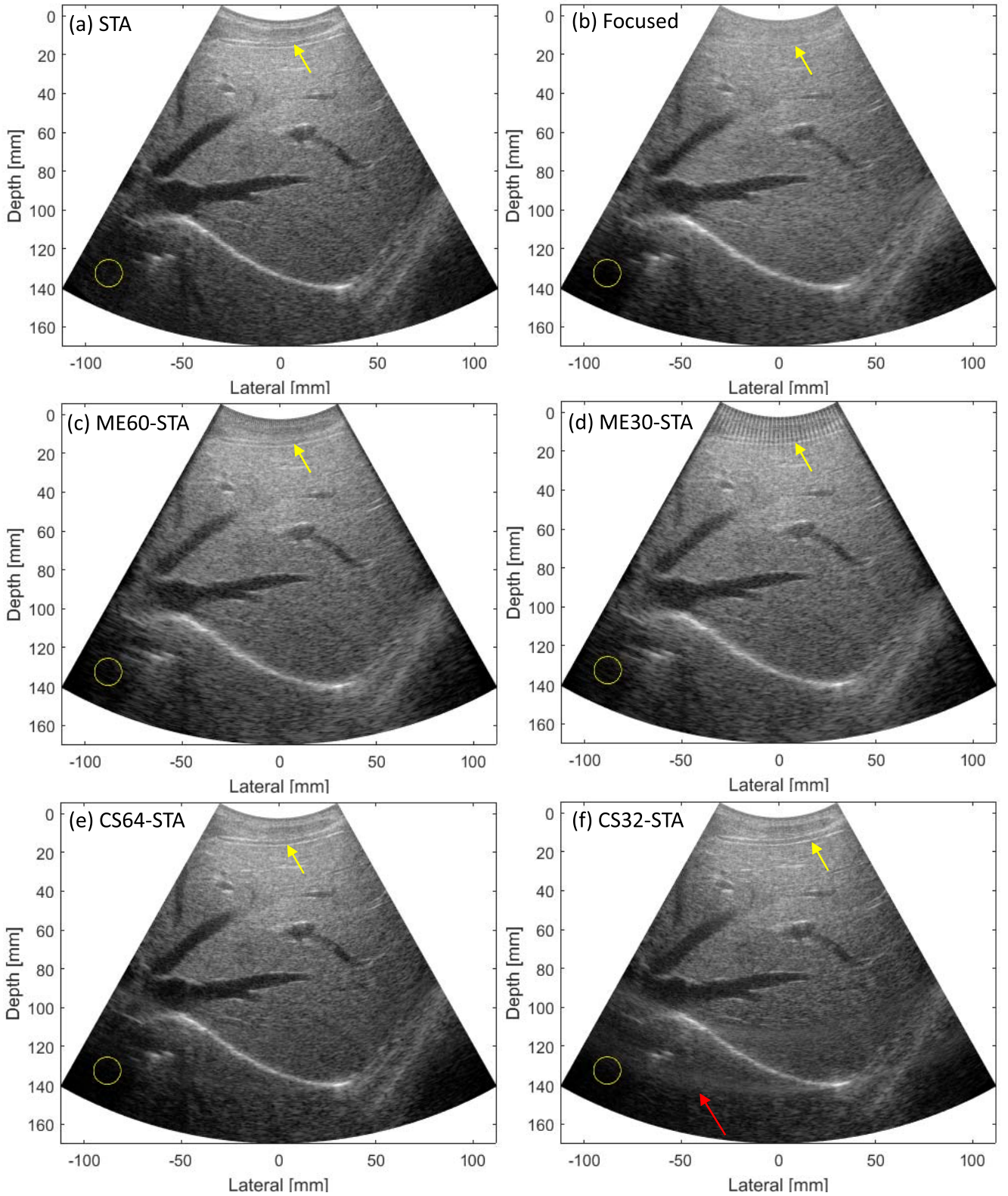


Fig. 11. B-mode images of different methods for the liver of a healthy male volunteer with a 70-dB dynamic range.

CS32-STA image in Fig. 8]. Besides, the artifacts along the lateral direction become more obvious when there are targets with very high reflectivity, which can be seen in Fig. 11(f). These artifacts can be reduced by increasing the number of DW firings, as shown in the results of simulations and phantom experiments [Fig. 4(b)–(d) and the CS64-STA image

of Figs. 8(e) and 11(e)]. That is to say, there is a tradeoff between the image quality and the number of firings (i.e., frame rate) in CS-STA. A similar tradeoff widely exists in ultrasound imaging. However, the benefit from CS-STA is a better image quality at large depths when the same (or similar) number of firings is used, as presented in Table I. It needs to

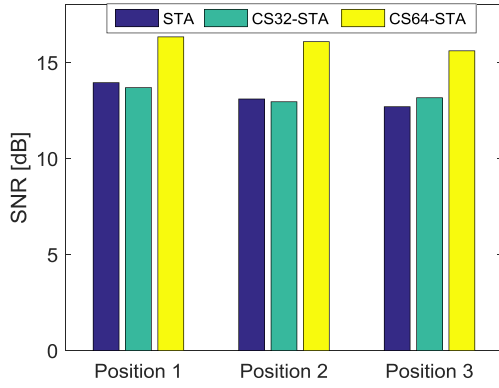


Fig. 12. Mean SNR of the hyperechoic region at the depth of 110 mm for STA and CS-STA calculated from three experiments.

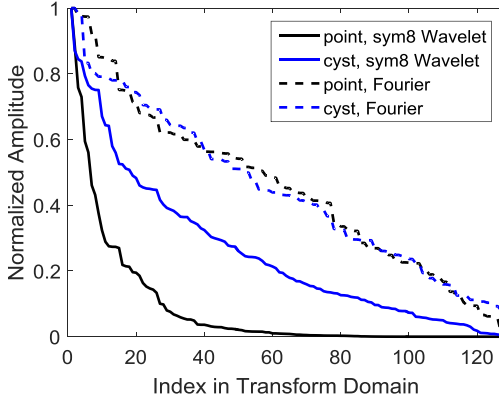


Fig. 13. Sorted normalized absolute amplitudes of  $\mathbf{v}$  in the *sym8* wavelet and Fourier bases for different phantoms.

be noted that although the TGC settings are the same for all the imaging modes, TGC can be adjusted to an optimal value for a specific imaging mode to achieve better image quality. Recently, an optimized synthetic focusing method has been proposed to achieve high resolution of convex array imaging by transmitting plane waves with different steering angles [47], which may be compared with CS-STA in the future.

The performance of CS-STA is highly related to the CS reconstruction. When the reconstruction algorithm is determined, it is related to the sparsity of the original signal and the incoherence between the measurement matrix  $\Phi$  and the sparse basis  $\Psi$ . The sparser the original signal is, the better the recovery performance CS-STA achieves. The sparse properties of the slow time signals of STA firing from different phantoms with the *sym8* wavelet and Fourier bases are shown in Fig. 13, by plotting the sorted normalized absolute amplitudes of the associated coefficients  $\mathbf{v}$ . It is found that the slow time signal of STA firing in the *sym8* wavelet domain decays faster than those in the Fourier domain. That is to say, the slow time signal of STA firing has a sparser representation with *sym8* wavelet than with Fourier basis. Therefore, *sym8* wavelet basis is used in this paper. It is a rather coarse choice but obtains satisfactory results. To achieve better recovery performance, the learned overcomplete dictionary, which has been reported to represent signal sparser due to the optimization learning process [20], will be adopted in our future work. Fig. 13 also shows that the signal from the point phantom is sparser than that from the cyst phantom when the *sym8* basis is used. The effect of sparsity can be seen in Fig. 3, where the NRMSEs of

the cyst phantom are higher than those of the point phantom because of the lower sparsity, which is the same as the linear array case [21]. In this paper, the coherence between the measurement matrix  $\Phi$  and *sym8* wavelet sparse basis is about 2.46, close to the coherence 2.2 between noiselets and Daubechies D4 wavelet [2]. It demonstrates that  $\Phi$  and  $\Psi$  are incoherent, which guarantees the successful reconstruction of CS-STA.

Another criterion to evaluate the performance of CS-STA is the reconstruction time. As Section II describes, the CS reconstruction is repeated for all receive elements and samples to recover the full STA channel data set. In the phantom experiments, when the imaging depth is 130 mm and the sampling frequency is 12.5 MHz, there are about 2110 samples for each channel and the CS reconstruction is repeated for  $128 \times 2110$  times. In our experiments, each CS reconstruction took about 0.3 s in MATLAB 2013a (The MathWorks, Inc., Natick, MA, USA) on a notebook computer (Intel Core i7-4610M CPU at 3 GHz, 16-GB RAM) and the total CS reconstruction time was about 22 h. The computational time of CS reconstruction may be reduced by using more efficient CS algorithms. In addition, the full CS-STA reconstruction procedure is suitable to be processed in parallel because each CS reconstruction is independent. With the help of parallel computation, the reconstruction time of CS-STA can be reduced considerably. In our latest experiment, the reconstruction process was programmed in parallel in MATLAB language on Dell XPS 8500 [Intel Core i7-3770 CPU at 3.40 GHz, 8-GB RAM]. The CPU has four cores with eight threads. The modified code ran on four cores in parallel and the reconstruction time was reduced to about 4.6 h. We believe that the reconstruction time will not be an obstacle with the development of computer and algorithm optimization.

### C. Applications

Section II-B derived the relationship between the channel data set of STA and that of DW firings. Although this derivation is for a slightly curved array and requires that the ultrasound pulse-echo transfer function is linear, the phantom and *in vivo* experiments have demonstrated that CS-STA is applicable for a real convex array and ultrasound system. Convex array is widely used in abdominal imaging and obstetrics, and the image depth is usually over 100 mm. Therefore, good image quality at large depths is crucial for ultrasound imaging with a convex array. The experimental results showed that CS-STA achieves good image quality (resolution, contrast, and CNR) at full depth. In addition, the frame rate of CS-STA was twice or four times higher than those of STA and the focused mode. This advantage is important when the abdominal organs move or new imaging methods such as shear wave elastography are implemented on a convex array [48]. However, the CS reconstruction may fail when the tissue motion is large enough, and then CS-STA may not be capable of imaging such tissues or tracking the shear wave. As a result, the effect of motion on CS-STA should be studied before it is applied to the imaging of moving tissues or shear wave elastography.

## VII. CONCLUSION

In this paper, we applied the theory of CS based STA to a slightly curved array with certain assumptions and validated it in a convex array configuration through simulations, phantom and *in vivo* experiments. The simulations demonstrated that CS-STA could recover the full STA channel data set with fewer firings (and thus increase the frame rate) in the convex array configuration. In addition, phantom experiments showed that CS-STA achieved good image quality (resolution, contrast, and CNR) at full depth, when compared with STA, ME-STA, and the conventional focused method. Similar results were also obtained in the *in vivo* experiments. CS-STA is thus proved to be capable of increasing the frame rate of ultrasound imaging and achieving high image quality at full depth in the convex array configuration.

## APPENDIX

Comparing (2) with (13), the original signal  $\mathbf{x}$  is extracted from the STA channel data set at a *specific* sample (e.g., the  $q^{\text{th}}$  sample) and receive channel (e.g., the  $j^{\text{th}}$  channel), while the measurement signal  $\mathbf{y}$  is extracted from the channel data set of CS-STA at the same sample and receive channel. The original STA signal  $\mathbf{x}$  can be recovered from the CS-STA signal  $\mathbf{y}$  by solving (6). By repeating this process for *all* the samples and receive channels, the full STA data set can be recovered.

The workflow of CS-STA can be summarized as follows.

*Step 1:* Obtain the measurement signal  $\mathbf{y}$  for a *specific* sample and receive channel, as the left of (13) shows.

*Step 2:* Recover the original signal  $\mathbf{x}$  for the *specific* sample and receive channel, using the CS method, particularly, by solving (6).

*Step 3:* Repeat the first two steps for *all* the samples and receive channels.

The MATLAB pseudocode is given as follows.

```
for sample=1:num_samples
for receive_channel=1: num_elements
    % CS reconstruction:
    % solve Eq. (6)
    y (sample, receive_channel) → v (sample,
    receive_channel);
    % substitute to Eq. (1)
    v (sample, receive_channel) → x (sample,
    receive_channel);
end
end
```

For each sample and receive channel, the recovery of the original STA signal  $\mathbf{x}$  from the CS-STA signal  $\mathbf{y}$  is the CS problem to be solved. It is an optimization problem as (6) describes. In this paper, the SPGL1 solver is employed to solve (6).

SPGL1 is an MATLAB solver for large-scale one-norm regularized least squares, developed by Dr. Michael P. Friedlander at the University of California, Davis (available at <https://www.math.ucdavis.edu/~mpf/spgl1/index.html>). The theory underlying SPGL1 is beyond the scope of this paper and can be found in [43] and [44]. It is designed to solve any of the following three problems.

*Problem 1 (Basis Pursuit Denoise):*

$$\min \|\mathbf{x}\|_1 \quad \text{s.t.} \quad \|\mathbf{Ax} - \mathbf{b}\|_2 \leq \sigma. \quad (\text{A1})$$

*Problem 2 (Basis Pursuit):*

$$\min \|\mathbf{x}\|_1 \quad \text{s.t.} \quad \mathbf{Ax} = \mathbf{b}. \quad (\text{A2})$$

*Problem 3 (Lasso):*

$$\min \|\mathbf{Ax} - \mathbf{b}\|_2 \quad \text{s.t.} \quad \|\mathbf{x}\| \leq \tau. \quad (\text{A3})$$

As can be seen, (6) is in the form of Problem 1. In this paper, SPGL1 is used to obtain the sparse representation  $\mathbf{v}$  of the original signal  $\mathbf{x}$ . By substituting  $\mathbf{v}$  into (1), the original signal  $\mathbf{x}$  can be recovered. By repeating this process for all the samples and receive channels, the full STA channel data set can be recovered with a smaller number of firings.

## REFERENCES

- [1] D. L. Donoho, "Compressed sensing," *IEEE Trans. Inf. Theory*, vol. 52, no. 4, pp. 1289–1306, Apr. 2006.
- [2] E. J. Candès and M. B. Wakin, "An introduction to compressive sampling," *IEEE Signal Process. Mag.*, vol. 25, no. 2, pp. 21–30, Mar. 2008.
- [3] M. Lustig, D. Donoho, and J. M. Pauly, "Sparse MRI: The application of compressed sensing for rapid MR imaging," *Magn. Reson. Med.*, vol. 58, no. 6, pp. 1182–1195, 2007.
- [4] M. A. Herman and T. Strohmer, "High-resolution radar via compressed sensing," *IEEE Trans. Signal Process.*, vol. 57, no. 6, pp. 2275–2284, Jun. 2009.
- [5] G.-H. Chen, J. Tang, and S. Leng, "Prior image constrained compressed sensing (PICCS): A method to accurately reconstruct dynamic CT images from highly undersampled projection data sets," *Med. Phys.*, vol. 35, no. 2, pp. 660–663, 2008.
- [6] J. Provost and F. Lesage, "The application of compressed sensing for photo-acoustic tomography," *IEEE Trans. Med. Imag.*, vol. 28, no. 4, pp. 585–594, Apr. 2009.
- [7] Z. Guo, C. Li, L. Song, and L. V. Wang, "Compressed sensing in photoacoustic tomography *in vivo*," *J. Biomed. Opt.*, vol. 15, no. 2, Mar. 2010, Art. no. 021311.
- [8] M. F. Duarte *et al.*, "Single-pixel imaging via compressive sampling," *IEEE Signal Process. Mag.*, vol. 25, no. 2, pp. 83–91, Mar. 2008.
- [9] A. C. Fannjiang, "Compressive inverse scattering: II. Multi-shot SISO measurements with born scatterers," *Inverse Problems*, vol. 26, no. 3, Mar. 2010, Art. no. 035009.
- [10] A. C. Fannjiang, "Compressive inverse scattering: I. High-frequency SIMO/MISO and MIMO measurements," *Inverse Problems*, vol. 26, no. 3, Mar. 2010, Art. no. 035008.
- [11] M. F. Schiffrer and G. Schmitz, "Fast pulse-echo ultrasound imaging employing compressive sensing," in *Proc. IEEE Int. Ultrason. Symp. (IUS)*, Oct. 2011, pp. 688–691.
- [12] R. Tur, Y. C. Eldar, and Z. Friedman, "Innovation rate sampling of pulse streams with application to ultrasound imaging," *IEEE Trans. Signal Process.*, vol. 59, no. 4, pp. 1827–1842, Apr. 2011.
- [13] C. Quinsac, A. Basarab, and D. Kouamé, "Frequency domain compressive sampling for ultrasound imaging," *Adv. Acoust. Vibrat.*, vol. 2012, Apr. 2012, Art. no. 231317, doi: 10.1155/2012/231317.
- [14] N. Wagner, Y. C. Eldar, and Z. Friedman, "Compressed beamforming in ultrasound imaging," *IEEE Trans. Signal Process.*, vol. 60, no. 9, pp. 4643–4657, Sep. 2012.
- [15] M. Shen, Q. Zhang, D. Li, J. Yang, and B. Li, "Adaptive sparse representation beamformer for high-frame-rate ultrasound imaging instrument," *IEEE Trans. Instrum. Meas.*, vol. 61, no. 5, pp. 1323–1333, May 2012.
- [16] H. Liebgott, R. Prost, and D. Friboulet, "Pre-beamformed RF signal reconstruction in medical ultrasound using compressive sensing," *Ultrasonics*, vol. 53, pp. 525–533, Feb. 2013.
- [17] T. Chernyakova and Y. Eldar, "Fourier-domain beamforming: The path to compressed ultrasound imaging," *IEEE Trans. Ultrason., Ferroelect., Freq. Control*, vol. 61, no. 8, pp. 1252–1267, Aug. 2014.
- [18] G. David, J.-I. Robert, B. Zhang, and A. F. Laine, "Time domain compressive beam forming of ultrasound signals," *J. Acoust. Soc. Amer.*, vol. 137, pp. 2773–2784, May 2015.



- [19] C. Wang *et al.*, "An easily-achieved time-domain beamformer for ultrafast ultrasound imaging based on compressive sensing," in *Proc. 37th Annu. Int. Conf. IEEE Eng. Med. Biol. Soc. (EMBC)*, Aug. 2015, pp. 7490–7493.
- [20] O. Lortintu, H. Liebgott, M. Alessandrini, O. Bernard, and D. Friboulet, "Compressed sensing reconstruction of 3D ultrasound data using dictionary learning and line-wise subsampling," *IEEE Trans. Med. Imag.*, vol. 34, no. 12, pp. 2467–2477, Dec. 2015.
- [21] J. Liu, Q. He, and J. Luo, "A compressed sensing strategy for synthetic transmit aperture ultrasound imaging," *IEEE Trans. Med. Imag.*, to be published, doi: 10.1109/TMI.2016.2644654.
- [22] G. Montaldo, M. Tanter, J. Bercoff, N. Benech, and M. Fink, "Coherent plane-wave compounding for very high frame rate ultrasonography and transient elastography," *IEEE Trans. Ultrason., Ferroelectr., Freq. Control*, vol. 56, no. 3, pp. 489–506, Mar. 2009.
- [23] J. Bercoff *et al.*, "Ultrafast compound Doppler imaging: Providing full blood flow characterization," *IEEE Trans. Ultrason., Ferroelectr., Freq. Control*, vol. 58, no. 1, pp. 134–147, Jan. 2011.
- [24] J. Udesen, F. Gran, K. L. Hansen, J. A. Jensen, C. Thomsen, and M. B. Nielsen, "High frame-rate blood vector velocity imaging using plane waves: Simulations and preliminary experiments," *IEEE Trans. Ultrason., Ferroelectr., Freq. Control*, vol. 55, no. 8, pp. 1729–1743, Aug. 2008.
- [25] M. Cikes, L. Tong, G. R. Sutherland, and J. D'hooge, "Ultrafast cardiac ultrasound imaging: Technical principles, applications, and clinical benefits," *Cardiovascular Imag.*, vol. 7, no. 8, pp. 812–823, Aug. 2014.
- [26] C. Papadacci, M. Pernot, M. Couade, and M. Fink, "High-contrast ultrafast imaging of the heart," *IEEE Trans. Ultrason., Ferroelectr., Freq. Control*, vol. 61, pp. 288–301, Feb. 2014.
- [27] B. D. Steinberg, "Digital beamforming in ultrasound," *IEEE Trans. Ultrason., Ferroelectr., Freq. Control*, vol. 39, no. 6, pp. 716–721, Nov. 1992.
- [28] A. Achim, B. Buxton, G. Tzagkarakis, and P. Tsakalides, "Compressive sensing for ultrasound RF echoes using a-stable distributions," in *Proc. 32nd Annu. Int. Conf. IEEE Eng. Med. Biol. Soc. (EMBC)*, Aug. 2010, pp. 4304–4307.
- [29] D. Friboulet, H. Liebgott, and R. Prost, "Compressive sensing for raw RF signals reconstruction in ultrasound," in *Proc. IEEE Int. Ultrason. Symp. (IUS)*, Oct. 2010, pp. 367–370.
- [30] C. Quinsac, A. Basarab, J. Girault, and D. Kouame, "Compressed sensing of ultrasound images: Sampling of spatial and frequency domains," in *Proc. IEEE Workshop Signal Process. Syst. (SIPS)*, Oct. 2012, pp. 231–236.
- [31] J. A. Jensen, S. I. Nikolov, K. L. Gammelmark, and M. H. Pedersen, "Synthetic aperture ultrasound imaging," *Ultrasonics*, vol. 44, pp. e5–e15, Dec. 2006.
- [32] M. F. Schiffner and G. Schmitz, "Compensating the combined effects of absorption and dispersion in plane wave pulse-echo ultrasound imaging using sparse recovery," in *Proc. IEEE Int. Ultrason. Symp. (IUS)*, Jul. 2013, pp. 573–576.
- [33] E. J. Candès, J. Romberg, and T. Tao, "Robust uncertainty principles: Exact signal reconstruction from highly incomplete frequency information," *IEEE Trans. Inf. Theory*, vol. 52, no. 2, pp. 489–509, Feb. 2006.
- [34] E. J. Candès and T. Tao, "Decoding by linear programming," *IEEE Trans. Inf. Theory*, vol. 51, no. 12, pp. 4203–4215, Dec. 2005.
- [35] E. J. Candès, "The restricted isometry property and its implications for compressed sensing," *Comp. Rendus Math.*, vol. 346, nos. 9–10, pp. 589–592, May 2008.
- [36] J. A. Tropp and A. C. Gilbert, "Signal recovery from random measurements via orthogonal matching pursuit," *IEEE Trans. Inf. Theory*, vol. 53, no. 12, pp. 4655–4666, Dec. 2007.
- [37] S. S. Chen, D. L. Donoho, and M. A. Saunders, "Atomic decomposition by basis pursuit," *SIAM J. Sci. Comput.*, vol. 20, no. 1, pp. 33–61, 1999.
- [38] J. A. Jensen, "A model for the propagation and scattering of ultrasound in tissue," *J. Acoust. Soc. Amer.*, vol. 89, pp. 182–190, Jan. 1991.
- [39] J. A. Jensen and N. B. Svendsen, "Calculation of pressure fields from arbitrarily shaped, apodized, and excited ultrasound transducers," *IEEE Trans. Ultrason., Ferroelectr., Freq. Control*, vol. 39, no. 2, pp. 262–267, Mar. 1992.
- [40] A. Penttinen and M. Luukkala, "The impulse response and pressure nearfield of a curved ultrasonic radiator," *J. Phys. D, Appl. Phys.*, vol. 9, no. 10, pp. 1547–1557, 1976.
- [41] J. A. Jensen, "Field: A program for simulating ultrasound systems," in *Proc. 10th Nordic-Baltic Conf. Biomed. Imag.*, 1996, pp. 351–353.
- [42] E. van den Berg and M. P. Friedlander. (2007). *SPGL1: A Solver for Large-Scale Sparse Reconstruction*. [Online]. Available: <https://www.math.ucdavis.edu/~mpf/spgl1/index.html>
- [43] E. van den Berg and M. P. Friedlander, "Probing the Pareto frontier for basis pursuit solutions," *SIAM J. Sci. Comput.*, vol. 31, no. 2, pp. 890–912, 2008.
- [44] E. van den Berg and M. P. Friedlander, "Sparse optimization with least-squares constraints," *SIAM J. Optim.*, vol. 21, no. 4, pp. 1201–1229, 2011.
- [45] Y. Tasinkevych, I. Trots, A. Nowicki, and P. A. Lewin, "Modified synthetic transmit aperture algorithm for ultrasound imaging," *Ultrasonics*, vol. 52, no. 2, pp. 333–342, Feb. 2012.
- [46] Y. Tasinkevych, Z. Klimonda, M. Lewandowski, A. Nowicki, and P. A. Lewin, "Modified multi-element synthetic transmit aperture method for ultrasound imaging: A tissue phantom study," *Ultrasonics*, vol. 53, no. 2, pp. 570–579, 2013.
- [47] S. Bae, P. Kim, J. Kang, and T.-K. Song, "An optimized plane wave synthetic focusing imaging for high-resolution convex array imaging," in *Proc. IEEE Int. Ultrason. Symp. (IUS)*, Oct. 2015, pp. 1–4.
- [48] P. Song, M. W. Urban, A. Manduca, J. F. Greenleaf, and S. Chen, "Coded excitation plane wave imaging for shear wave motion detection," *IEEE Trans. Ultrason., Ferroelectr., Freq. Control*, vol. 62, no. 7, pp. 1356–1372, Jul. 2015.



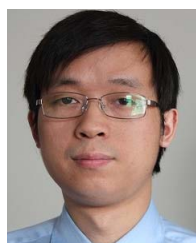
**Jing Liu** was born in Hubei, China, in 1990. She received the bachelor's degree in biomedical engineering from the Huazhong University of Science and Technology, Wuhan, China, in 2013. She is currently pursuing the Ph.D. degree with the Department of Biomedical Engineering, Tsinghua University, Beijing, China.

Her current research interests include ultrasound beamforming and compressed sensing applications in ultrasound imaging.



**Qiong He** was born in Henan, China, in 1989. She received the bachelor's degree in biomedical engineering from Capital Medical University, Beijing, China, in 2012. She is currently pursuing the Ph.D. degree with the Department of Biomedical Engineering, Tsinghua University, Beijing, China.

Her current research interests include signal processing for high-frame-rate cardiovascular imaging and shear wave elastography.



**Jianwen Luo** (S'02–M'06–SM'14) received the B.S. and Ph.D. (Hons.) degrees in biomedical engineering from Tsinghua University, Beijing, China, in 2000 and 2005, respectively.

He was a Post-Doctoral Research Scientist from 2005 to 2009 and an Associate Research Scientist from 2009 to 2011 with the Department of Biomedical Engineering, Columbia University, New York, NY, USA. He was a Professor with the Department of Biomedical Engineering and the Center for Biomedical Imaging Research, Tsinghua University,

in 2011. He has authored or coauthored over 110 peer-reviewed papers in international journals, 50 conference proceedings papers, and 120 conference abstracts. His current research interests include ultrasound imaging and fluorescence molecular imaging.

Dr. Luo serves as an Advisory Editorial Board Member of the *Journal of Ultrasound in Medicine*, and a member of the IEEE Engineering in Medicine and Biology Society and the Technical Committee on Biomedical Imaging and Image Processing. He was enrolled in the Thousand Young Talents Program of China in 2012, and received the Excellent Young Scientists Fund from the National Natural Science Foundation of China in 2013.